Physics – Uspekhi **60** (3) 276 – 289 (2017)

REVIEWS OF TOPICAL PROBLEMS

PACS numbers: **61.46.–w**, 61.66.Fn, **71.15.–m**, 71.15.Mb

High-melting-point compounds: new approaches and new results

R A Andrievski

DOI: https://doi.org/10.3367/UFNe.2016.09.037972

Contents

Abstract. **This paper reviews state-of-the-art research and new approaches in studying the field of high-melting point (> 2000 °C) compounds such as carbides, nitrides, borides, and oxides. New experimental and theoretical results on the structure, physical and mechanical properties and application of these compounds are described. Manufacturing aspects are reviewed, and research topics that have not been studied enough are identified.**

Keywords: refractory compounds, carbides, nitrides, borides, oxides

1. Introduction

The refractoriness concept, i.e., the property of having a high melting point, is blurred, both physically and physicochemically, with the value of about 2000 °C loosely adopted as the borderline for the melting temperature (T_{m}) [1]. Compounds commonly referred to as refractory include a large group of carbides, nitrides, borides, oxides, and intermetallics, as well as a number of silicides, phosphides, and sulfides — a total of about 170 phases. Clearly, covering all of these is beyond the scope of a single review paper, so we will primarily focus on metal-like carbides and nitrides (which are the most studied and of most engineering interest) and on dielectrics such as boron and silicon carbides and nitrides. There have also already been many monographs and reviews on the physical nature and properties of these compounds (see, for example, Refs [1–8]).

New approaches to studying nonstoichiometry and ordering [3, 8] and nanostructuring [4–6, 9, 10] in refractory compounds have already received sufficient attention. Thus, single-layer and multilayer films based on carbides, nitrides, and borides with a hardness of 50–80 GPa (i.e., at the level of the typical superhard materials diamond and boron nitride) were obtained in the late 1980s and early 1990s independently and virtually simultaneously by several groups in the US, Sweden, Former USSR, Germany, and Austria.

As an example, Fig. 1 demonstrates the effect of the number of layers on the hardness of TiN/NbN (*1*), TiN/ZrN (*2*), and TiN/CrN (*3*) films. For the first two cases, increasing the number of layers continuously increases the hardness due to the fact that dislocations and cracks are increasingly hindered in their motion as the number of interfaces they have to cross increases. The nonmonotonic change in the hardness of TiN/CrN films is associated with the formation of the solid solution (Ti, Cr)N in this system (as the lowest-temperature system in comparison with TiN–NbN and TiN–ZrN) and the disappearance of phase interfaces.

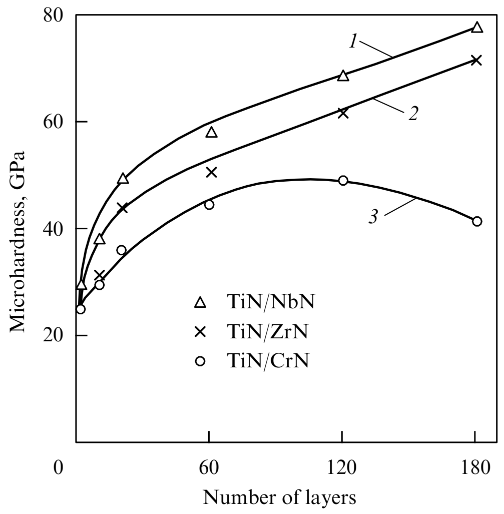

Figure 1. Microhardness of multilayer nitride films as a function of the number of layers.

R A Andrievski Institute of Problems of Chemical Physics,
Russian Academy of Sciences,
prosp. Akademika Semenova 1, 142432 Chernogolovka, Moscow region,
Russian Federation
E-mail: ara@icp.ac.ru

Received 21 April 2016, revised 29 July 2016
Uspekhi Fizicheskikh Nauk **187** (3) 296 – 310 (2017)
DOI: https://doi.org/10.3367/UFNr.2016.09.037972
Translated by E G Strel'chenko; edited by A Radzig

However, due attention has not yet been given to many other aspects of new approaches to studying the properties of refractory compounds. The focus of our attention here is on the characterization (in particular, the structure, properties, and promising application areas) and theoretical description of comparatively new objects.

2. New objects

2.1 *MAX* phases

While this term came from mid-1990s studies [11–13], similar phase compositions had been revealed much earlier in the analysis of ternary Ti–Si–C constitution diagrams. An *MAX* phase can be represented by a 'chemical formula' of the form $M_{n+1}AX_n$, where $n = 1, 2$, or 3, M is a transition metal, A is a nontransition element, and X is carbon or nitrogen. Figure 2 depicts schematically the unit cells of the M_2AX, M_3AX_2, and M_4AX_3 phases and shows the arrangement of the components in the Periodic Table [13].

Classified by the number of M, A, and X atoms in them, these phases are also commonly referred to as 211, 312, and 413. Although the structure and the physical and physicochemical properties of about 70 *MAX* phases have been described in detail in monograph [12] and in many reviews [13–15], the overwhelming majority of these compounds are not refractory. The most typical and most thoroughly studied high-melting-point *MAX* phase is Ti_3SiC_2, which forms in the

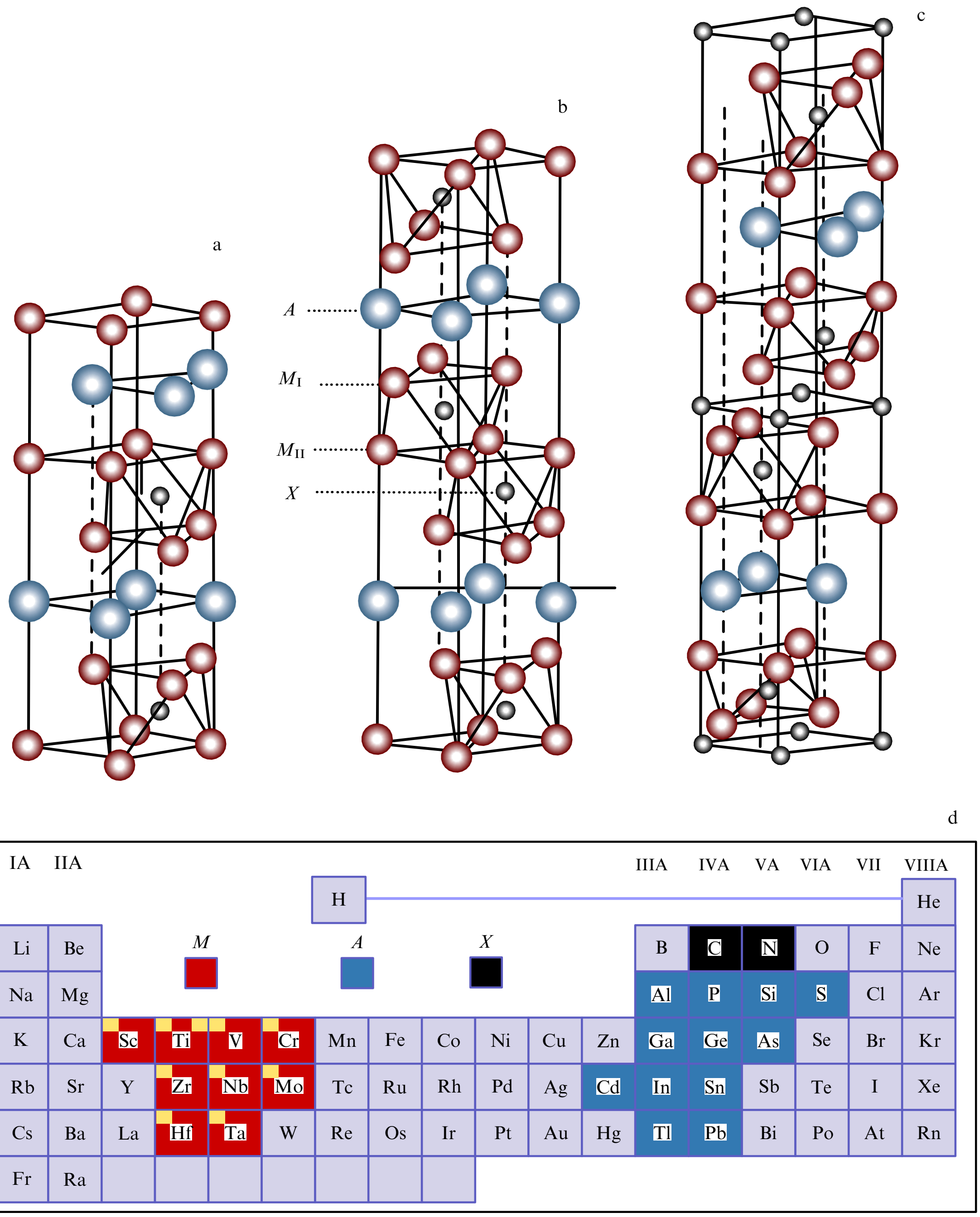

Figure 2. (Color online.) Unit cells of the phases M_2AX (a), M_3AX_2 (b), and M_4AX_3 (c) and the arrangement of the constituent components in the Periodic Table (d); M is a transition metal, A is a nontransition element, and X is carbon or nitrogen.

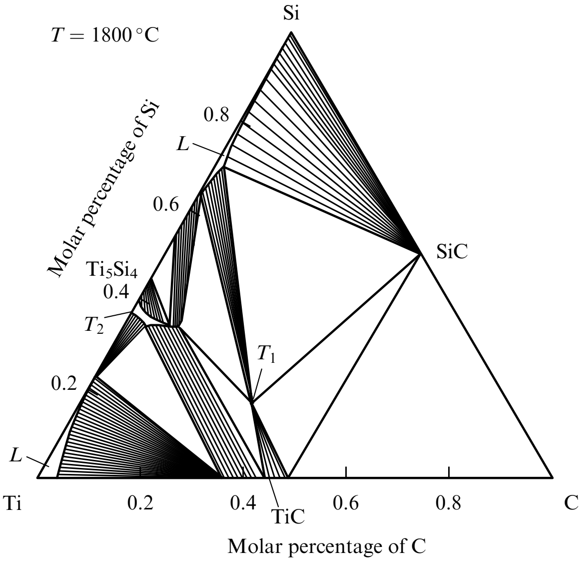

Figure 3. Calculated isothermal cross section of the Ti–Si–C phase diagram at $T = 1800\,°C$ (T_1 corresponds to Ti_3SiC_2, and T_2 corresponds to $Ti_5Si_3C_x$).

Ti–Si–C system (Fig. 3) and melts incongruently by a peritectic $M_3AX_2 \to M_3X_2 + A(\text{lqd})$ type reaction at a temperature of about 2300 °C [12, 16].

Considering the totality of their properties, the *MAX* phases are viewed as intermediate between typical metals and brittle compounds [13]. Table 1 collates the key characteristics of Ti_3SiC_2 with those of titanium and typical carbides (metal-like TiC and semiconducting SiC) [1, 12–14, 17–19]. It is seen that Ti_3SiC_2 characteristically has low electrical resistivity (combined with high electron heat capacity), considerably higher crack resistance, and a lower brittle-to-plastic transition temperature. While equal to titanium in terms of density, Ti_3SiC_2 carbide-silicide has a Young's modulus that is three times higher and possesses a significant stiffness and hardness. Its structure is charactristically stripe-patterned (laminar), with individual stripes measuring about 20 nm in thickness [19]. For samples with a grain size (L) of 5 μm, the compressive strength reaches 1050 MPa, and the tensile strength 300 MPa [13].

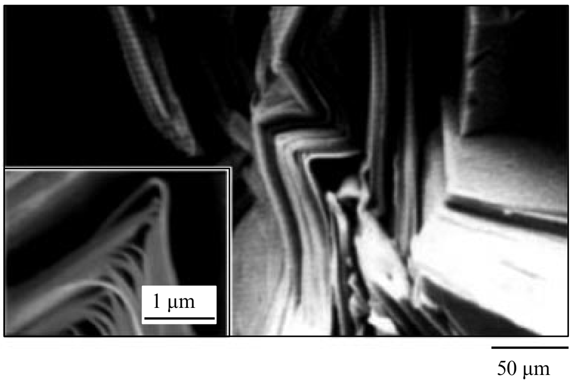

Figure 4. Scanning electron micrograph showing a fracture surface in Ti_3SiC_2.

In addition to the mechanical characteristics described, it should be noted that, unlike titanium and titanium carbide which obey the well-known von Mises rule (the occurrence of plasticity in the presence of five independent slip systems), shear deformation in Ti_3SiC_2 is constrained to three base plane directions, and the *MAX* phases exhibit quasiplasticity for $T > T_{bp}$ and under compression conditions. Figure 4 demonstrates the fracture surface of a strained Ti_3SiC_2 sample, in which the curving of the laminas and the formation of shear strips are seen [14].

Cyclic loading studies have revealed hysteresis characteristics to be weakly dependent on the number of cycles (at least in the range up to 100 cycles) and greatly dependent on the grain size (Fig. 5).

The mechanical properties of other *MAX* phases are also of interest, for example, of those synthesized by standard hot pressing methods or under high pressure–high temperature conditions in the Ti–Al–C(N) system [20–22]. Thus, for nanolaminated Ti_3AlC_2 compound (6% TiC and 5% Al_2O_3 layers, density of 4.27 g cm^{-3}, 1% porosity), the compressive (flexural) strength, microhardness, Young's modulus, and crack resistance are ~ 700 (~ 500) MPa, 2–4.6 GPa, 140 ± 29 GPa, and 4–10 MPa $m^{1/2}$, respectively.

It should be noted that the spread in the mechanical properties of the *MAX* phases is ascribed not only to the brittle nature of these compounds, but also to the basal plane

Table 1. Some physical, physicochemical, and mechanical properties of Ti, Ti_3SiC_2, TiC, and SiC.

Characteristic	Ti	Ti_3SiC_2	TiC	β-SiC
Crystal lattice	hcp (hexagonal close-packed)	Hexagonal	fcc (face-centered cubic)	Cubic
Density, g cm^{-3}	4.54	4.53	4.92	3.21
Melting point, °C	1660	~ 2300	3067 ($TiC_{0.8}$)	~ 2830
Resistivity (ρ) at $T = 20\,°C$, μΩ cm	45	23	60 – 150	$\sim 10^5$
Electron heat capacity coefficient, mJ mol^{-1} K^{-2}	3.35	6.4	0.5 – 1	—
Young's modulus (E), GPa	110	325 – 345	300 – 500	400 – 500
Microhardness (H_V), GPa	1	3 – 7	20 – 30	20 – 25
Crack resistance (K_{IC}), MPa $m^{1/2}$	no data	5 – 16	2 – 3	2 – 4
Brittle-to-plastic transition temperature (T_{bp}), °C	−268	1000 – 1100	1500	1800
Shear dislocation Burgers vector	1/3[−1 − 120], 1/3[0003]	1/3[11 − 20]	1/2[111], 1/2[110]	1/2[111]

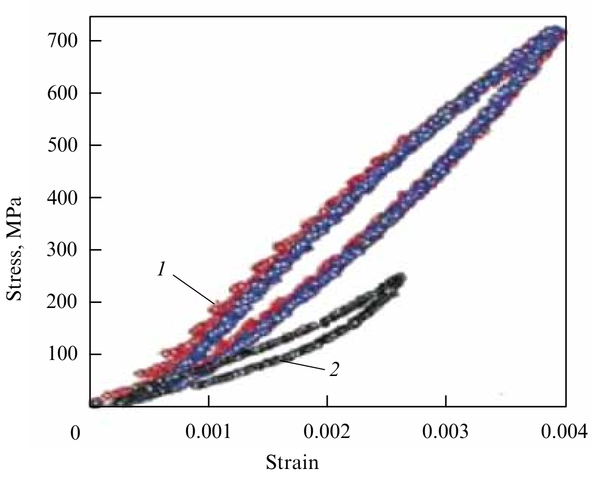

Figure 5. Strain hysteresis during the cyclic compression of Ti_3SiC_2 samples with a grain size $L \sim 5$ μm (*1*), and ~ 30 μm (*2*) [13].

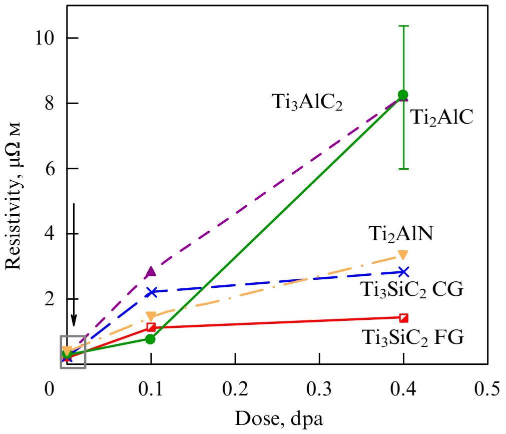

Figure 6. Resistivity as a function of the number of displacements per atom (dpa) in neutron irradiation for different titanium *MAX* phases. The arrow marks the value of ρ for virgin, nonirradiated objects. CG denotes coarse-grain samples ($L \sim 30$ μm), and FG denotes fine-grain samples ($L \sim 5$ μm).

orientation in individual grains, which changes the soft-to-stiff ratio in strained crystallites. Nonetheless, the characteristics of technological importance, such as the creep stability, thermal shock resistance (thermal strength), and mechanical processability, are sufficient to make the *MAX* phases promising for applications as heatproof materials [13].

In order to expand the range of potential applications, other properties (namely, corrosion, tribotechnological, and radiation) have been examined for many *MAX* phases. Among the findings was the high oxidation resistance of Ti_3SiC_2 at 900 °C, and of the compounds Ti_2AlC and Cr_2AlC even at 1300–1400 °C in the air [12]. Polycrystalline Ti_3SiC_2 samples have a low friction coefficient (below 0.15 over steel and silicon nitride), whereas the basal plane gives a friction coefficient of a record-breaking $(2-5) \times 10^{-3}$, a value which, in addition, proved to be stable for 6 months under atmospheric conditions [17].

Also, data on the radiation resistance of the *MAX* phases are also undoubtedly of interest. Figure 6 shows the effect of the neutron radiation dose (the integral fluence is 3.4×10^{20} n cm^{-2}, and energy is above 0.1 MeV) on the specific resistance of various compounds at 360 ± 20 °C [23]. As seen from these data, ρ of fine-grain T_3SiC_2 samples are influenced least by neuron irradiation. X-ray phase analysis (XPA), transmission electron microscopy (TEM), and high-resolution transmission electron microscopy (HRTEM) studies of the structure of irradiated samples showed the absence of amorphization but, on the other hand, revealed the development of dislocation loops and microckracks, as well as the decay of *MAX* phases into TiC and Al_2O_3. A similar, if less pronounced, effect of irradiation was observed for Ti_3SiC_2.

A qualitative comparison of how neutron irradiation influences the electrical resistivity of Ti_3SiC_2 and ZrC (TiC) samples [1, 24] (see Fig. 6) shows that an *MAX* phase suffers least irradiation damage among the usual transition metal carbides.

2.2 Two-dimensional *MX* phases

As is known, the term two-dimensional (2D) refers to objects with a large length-to-thickness ratio; two-dimensional *MX* phases are only a few atomic layers thick. The best-known and most widely studied 2D structure is graphene — hence, the term *MX*ene (i.e., analogous or similar to graphene) used in the literature abroad for two-dimensional *MX* phases. The way these phases are obtained is by selectively extracting (etching) nontransition atoms *A* from *MAX* phases followed by ultrasonic treatment. Figure 7 displays a schematic of how *MAX* phases transform into two-dimensional *MX* phases [25].

It turned out that the compounds most suitable for removing an *A* layer from *MAX* phases are those containing aluminum, so there are only a few known two-dimensional *MX* phases. Table 2 [25] presents some compounds obtained by etching nontransition metal atoms from *MAX* phases using a hydrofluoric acid solution. Experimental and theoretical studies have established the presence of F and O atoms and OH hydroxyl on the hydrophil surface of two-dimensional *MX* phases, thus introducing the notation T_X (terminations) into their formulas.

Table 2 shows that the original and derivative phases differ quite significantly in the value of the parameter *c* and that transitions to two-dimensional *MX* phases increase the electrical resistivity (Table 3) [26, 27].

Temperature dependence studies of resistivity have revealed that $Ti_3C_2T_X$ samples behave like typical metallic objects up to 100 K and only on decreasing the temperature further does their resistivity start to increase, the increase occurring by $\rho \sim \ln T$, a formula which corresponds to the weak localization model characteristic of 2D metals (Fig. 8) [26].

Depending on the technological regimes, two-dimensional *MX* samples come in a wide variety of forms, including powders, consolidated powder compacts, scales, stripes, spirals, nanotubes, films, and colloidal solutions [25–27]. Some of these objects may be seen in Fig. 9.

Because of their promise for energy conservation applications, the study of two-dimensional *MX* phases is to a large extent concerned with their electrochemical properties. Reference [28] describes changes in the elastic properties of $Ti_3C_2T_X$ electrodes caused by electrochemical intercalation (extraction of Li^+ and K^+ ions). Still, it should be noted that, compared to *MAX* phases, their *MX* derivatives have been much less studied experimentally. As also noted in review [25], more extended research is needed to obtain information on the physical, physicochemical, and mechanical properties of two-dimensional *MX* phases.

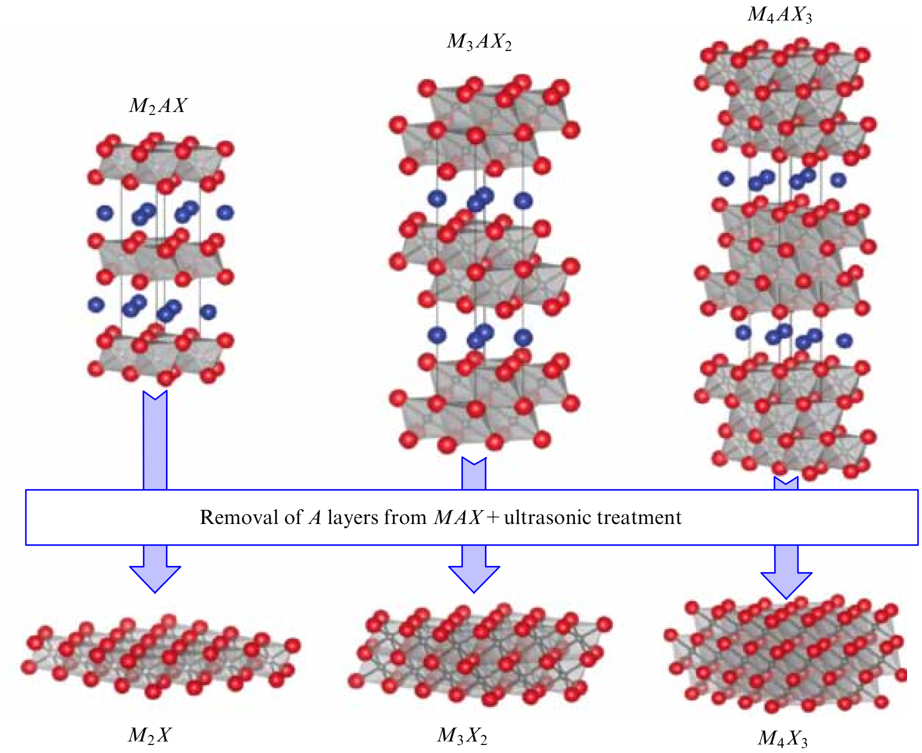

Figure 7. (Color online.) Transformation of MAX phases into two-dimensional MX phases (schematic). Nonmetallic atoms X (nitrogen or carbon) occupy the octahedral interstitials in hexagonal cells.

Table 2. Some crystallochemical characteristics of MAX phases and two-dimensional MX phases.

Notation of MAX phase	Formula and parameter c, Å			
	MAX	c	MX	c
211	Ti_2AlC V_2AlC Nb_2AlC $(Ti_{0.5}Nb_{0.5})_2AlC$	13.6 13.13 13.88 13.79	Ti_2CT_X V_2CT_X Nb_2CT_X $(Ti_{0.5}Nb_{0.5})_2CT_X$	15.04 19.73 – 23.96 22.34 14.88
312	Ti_3AlC_2 $(V_{0.5}Cr_{0.5})_3AlC_2$ Ti_3AlCN	18.42 – 18.62 17.73 18.41	$Ti_3C_2T_X$ $(V_{0.5}Cr_{0.5})_3C_2T_X$ Ti_3CNT_X	20.51 – 20.89 24.26 22.28
413	Ta_4AlC_3 Nb_4AlC_3	24.08 24.19	$Ta_4C_3T_X$ $Nb_4C_3T_X$	30.34 30.47

Table 3. Electrical properties of some MAX and MX phases.

Compound	Film thickness, nm	Resistivity at $T = 20\,°C$, μΩ cm
Ti_3AlC_2 $Ti_3C_2T_X$	15 – 60 17 – 67	31 – 45 176 – 3923
Nb_2AlC Nb_2CT_X Nb_4AlC_3 $Nb_4C_3T_X$	680 430 650 380	2×10^3 6.1×10^7 3.3×10^4 4.6×10^5
$Ta_4C_3T_X$	~ 300	2.1×10^6

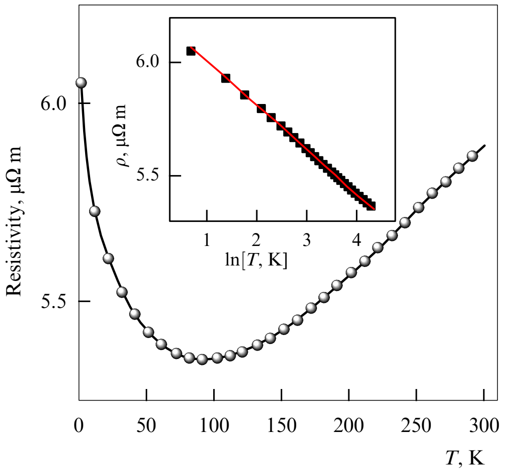

Figure 8. Resistivity vs temperature for 28-nm thick $Ti_3C_2T_X$ films. Inset: temperature dependence of $\rho \sim \ln T$ in the temperature range 2–74 K.

2.3 Two-dimensional boron nitride

Boron nitride (BN) has long attracted the attention of the science and engineering communities whether as a superhard material in its sphalerite- or wurtzite-like modifications or as an insulator analogous to hexagonal graphite. The advent of graphene with its remarkable properties [29] generated interest in finding other 2D-structured compounds — the immediate target being, naturally, graphene's closest analo-

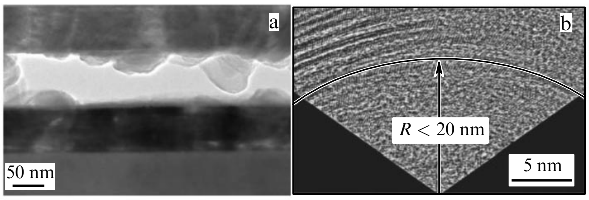

Figure 9. Transverse TEM (a) and HRTEM (b) images of a $Ti_3C_2T_X$ film and a spiral.

gue, boron nitride — and this topic has been the subject of much research effort, as summarized in a number of recent reviews (see, for example, Refs [30–35]).

Figure 10 illustrates the crystal structure and phase diagram of boron nitride [31]. The phase diagram does not show the wurtzite-like modification of BN, and the dots (● and ○) denote the measured values of T_m for different pressures, including 50 MPa (▲).

Similar to graphene, the two-dimensional strips of hexagonal boron nitride are obtained by mechanical and chemical layering methods and by deposition from a gas phase. Figure 11 presents electron micrographs of gas phase-deposited BN strips [31].

Figure 11a reveals the presence of bent strips; the interlayer distance for the strips is 0.33–0.34 nm, and the lattice parameters a and c are 0.250 nm and 0.666 nm, respectively, very close to those for graphite. Because such objects are difficult to study, only moderate information is available on experimental research into the properties of two-dimensional BN. Figure 12a is a schematic of a bending test setup for BN nanostrips using an atomic force microscope cantilever — a technique that provides an SEM image; Fig. 12b illustrates the effect of the sample size on the Young's modulus [36].

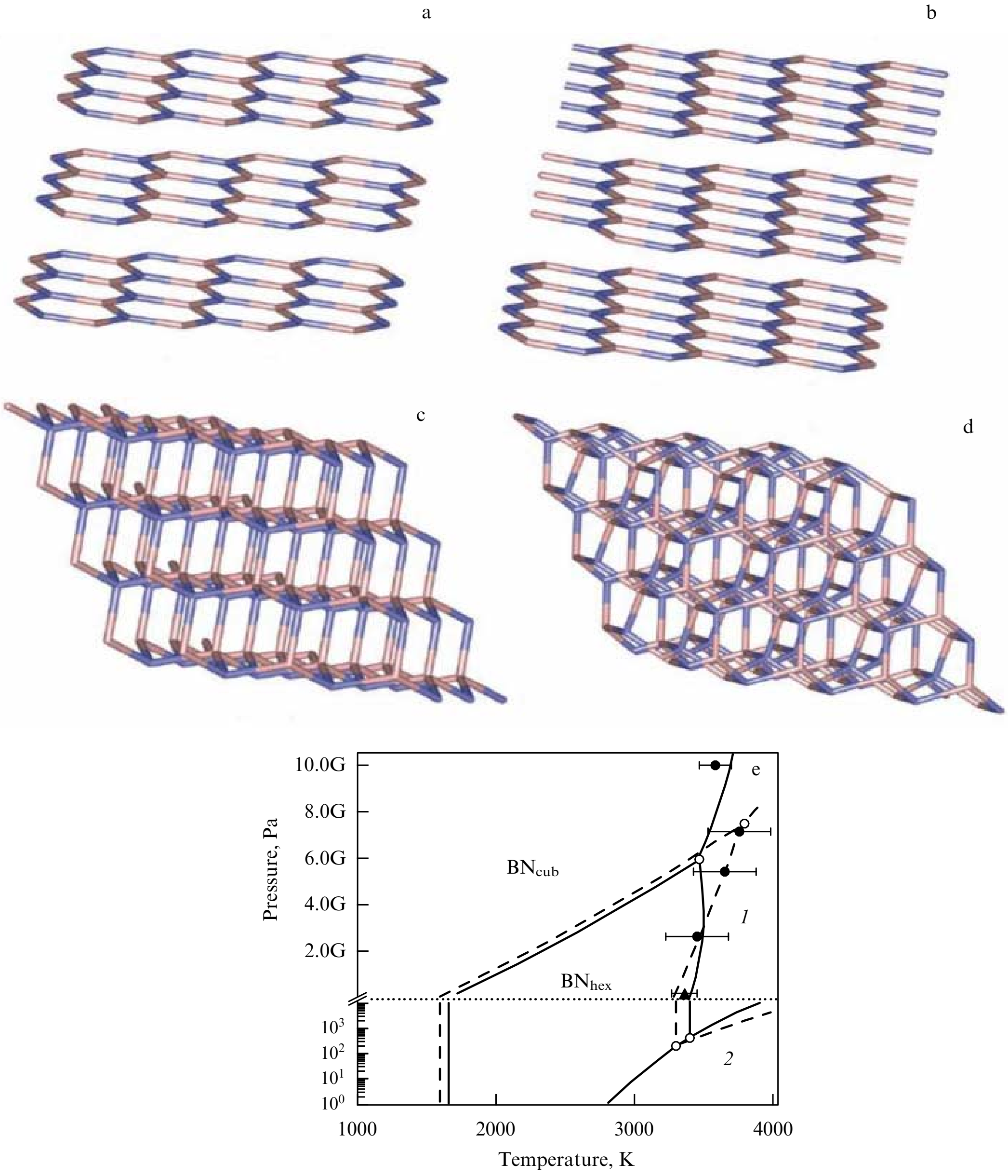

Figure 10. (Color online.) Schematic of BN crystal structures: (a, b) basal planes of the hexagonal and rhombohedral structures; (c, d) sphalerite (cubic) and wurtzite-like (hexagonal) structures. (e) BN phase diagram. *1* and *2* denote the liquid and vapor regions; ordinate values of pressure above the dashed line are given in gigapascals.

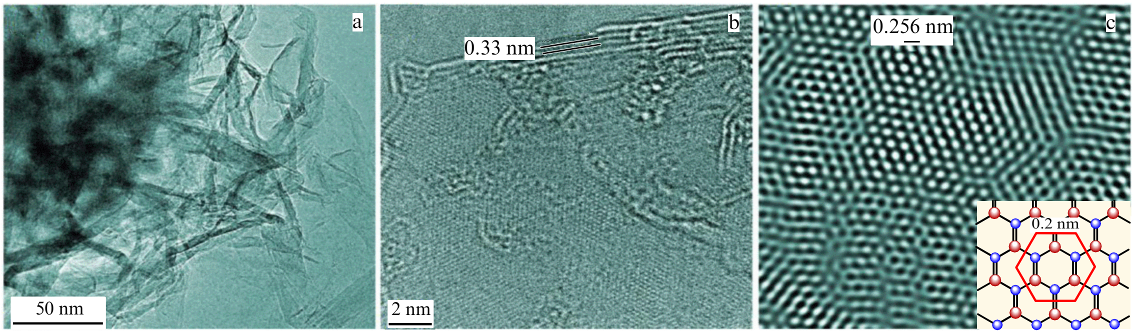

Figure 11. TEM (a) and HRTEM (b) images of boron nitride strips, and (c) its hexagonal lattice.

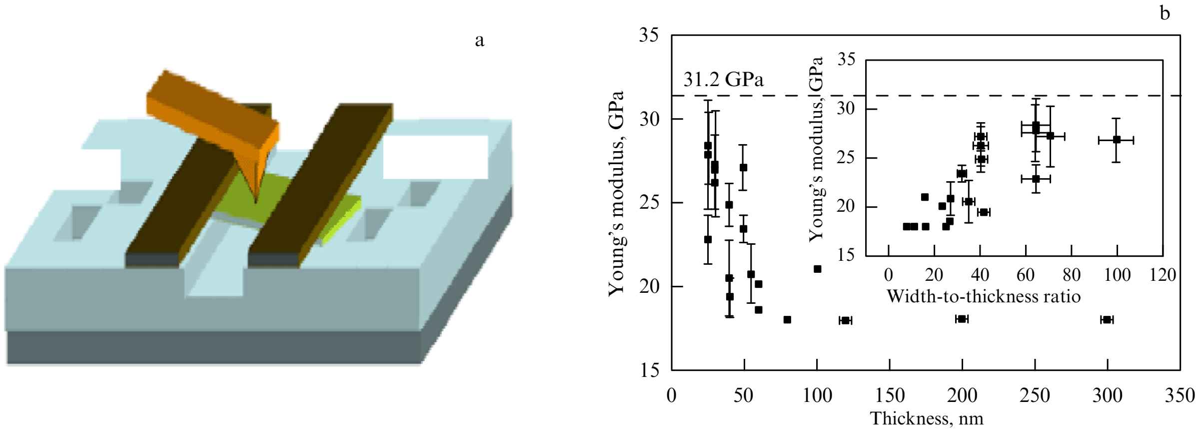

Figure 12. Schematic of a bending test setup (a) and the effect of the nanostrip size on Young's modulus (b). The horizontal dashed line indicates the value of *E* calculated in Ref. [37].

From Fig. 12b it is seen that the size effect is significant, and *E* can reach its theoretical value only for nanostrip thicknesses of less than appr. 40–50 nm. It should be noted that nanodimensional boron nitride can also be produced in other forms — fullerenes and nanoparticles (0D), nanotubes and nanoribbons (1D), and porous nanostructures (3D) — whose structure-sensitive properties may differ widely. The properties of two-dimensional BN and those of graphene were compared in detail in review [35], data from which are given in Table 4 augmented by some information on the characteristics of one-dimensional boron nitride.

Data in Table 4 imply that nanodimensional boron nitride, while virtually remaining a wide-band semiconductor, is in no way (except for the heat conductivity) inferior to metal-like graphene, while exceeding it in corrosion resistance. Also noted are the optical transparency over a wide frequency range and the high stress–strain, luminescent, and barrier-protection characteristics of BN [35].

Compared with nanoboron nitride, less information is available on the structure and properties of other layered refractory compounds (silicon carbide, boron carbonitride, sulfides, etc.); the reader is referred to Refs [30, 40, 41] for these data. It is also worthwhile to note that interest in two-dimensional materials is currently greatly increasing. Since 2014, *2D Materials* quarterly has been published by the IOP Science Publishing House of the American Institute of Physics, which is already reflected in the *WEB of Science* database.

2.4 High-entropy nitrides and carbides. High-entropy alloys in cermets

Since the work reported in Refs [42–44], there has also been an increased fundamental and applied interest in high-entropy alloys (HEAs) — compounds which contain no less than five substitutional components, none of them dominant. The HEA design ideology is that the sufficiently high configurational mixing entropy (given by the well-known formula $R \ln n$, where R is the molar gas constant, and n is the number of components) ensures the formation of a disordered solid solution and makes intermetallic phases thermodynamically

Table 4. Some properties of nanodimensional boron nitride and graphene.

Object	Bandgap energy, eV	Resistivity, Ω cm	Heat conductivity, $W m^{-1} K^{-1}$	Young's modulus, GPa	Breaking strength, MPa	Breaking strain, %	Oxidation onset temperature, °C
1D-BN	~ 6	$(7.1 \pm 0.9) \times 10^4$ [38]	100 – 270	725 – 1343 [39]	14 – 33 [39]	1.5 – 3.4 [39]	800
2D-BN		no data		25 – 28 [36]	120 – 165	no data	
Graphene	semimetal	at a level of ~ 10^{-4}	1800 – 5400	1000	130	no data	450

Table 5. Mechanical properties of some HEA nitrides and carbides.

Phase	H_V, GPa	E, GPa	References
(Al,Cr,Ta,Ti,Zr)N	36	360	[49]
(Al,Cr,Mo,Si,Ti)N	35	325	[50]
(Al,Cr,Si,Ti,V)N	31	300	[51]
(Al,B,Cr,Si,Ti)N	25	260	[52]
(Al,Cr,Nb,Si,Ti,V)N	42	350	[53]
(Al,Mo,Nb,Si,Ta,Ti,V,Zr)N	37	350	[54]
(Hf,Nb,Ti,V,Zr)N	50 – 60	580 – 660	[55]
(Al,Nb,Ti,Zr,Y)N	34 – 49	no data	[56]
(Hf,Nb,Ta,Ti,V,Zr)N	~ 35	~ 300	[57]
(Al,Cr,Ta,Ti,Zr)C	40	303	[45]
(Cr,Nb,Si,Ti,Zr)C	33	360	[45]

Table 6. Structural parameters and properties of an HEA, its nitride and carbide, and TiN and TiC (a is the fcc lattice parameter, L is the grain size, ε is the lattice strain, H_V is the microhardness, μ is the friction coefficient, and K is the specific wear equal to wear indentation volume divided by the force and slippage length) [60].

Film type	a, nm	L, nm	ε	H_V, GPa	μ	$K \times 10^{-6}$, mm^3 H^{-1} m^{-1}
Hf – Nb – Ta – Ti – Zr	0.420	18	0.004	5.4	0.87	17
(Hf,Nb,Ta,Ti,Zr)$N_{1,1}$	0.446	7	0.013	32.9	0.96	2.9
(Hf,Nb,Ta,Ti,Zr)$C_{1,1}$	0.460	5	0.024	27.5	0.15	0.8
$TiN_{1,08}$	0.424	17	0.004	23.1	0.84	4.4
$TiC_{1,23}$	0.425	9	0.010	21.6	0.18	9.4

unfavorable. This leads to emerging considerable lattice distortions and slows down diffusion processes and phase transformations in the crystal, causing favorable changes in the physicomechanical and physicochemical properties of HEAs, as discussed in numerous literature sources, of which we will limit ourselves to referring to a few recent ones, e.g., Refs [45–48].

In relation to high-melting-point compounds, the focus is primarily on HEA nitride films obtained either by magnetron sputtering or vacuum arc vaporization [45, 46]; for carbide compounds, only partial research has been conducted. Table 5 lists the values of microhardness and Young's modulus for some high-entropy nitrides and carbides.

It is noteworthy that the face-centered cubic (fcc) objects in Table 5 have a grain size of 5 to 50 nm. Of note is the good thermal stability (up to 900 °C) and the high air oxidation resistance (up to 1000 °C) of $(Al_{0.34}Cr_{0.22}Nb_{0.11}Si_{9.11}Ti_{0.22})_{59}N_{50}$ films [58, 59]. Reference [60] provides a detailed comparison of the structure and some properties of nitride and carbide films based on Hf–Nb–Ta–Ti–Zr HEA.

Table 6 presents information on the structure, hardness, friction coefficient, and wear of an HEA and its related carbide and nitride, and, for comparison, on the same properties of titanium nitride and carbide. Films of these materials were prepared by magnetron sputtering and had about the same thickness of 1.9–2.1 μm, thus ensuring the comparability of results.

Table 6 clearly shows the extent to which the hardness and wear change as a metallic HEA makes a transition to nitride and carbide alloys and how they differ from the usual parameters of TiN and TiC. However, to explore in more detail the role of the high entropy factor in shaping the properties of HEA-based nitrides and carbides, the data in Tables 5 and 6 should be analyzed using the known properties of nitride- and carbide-based nanostructure coatings (see, for example, Refs [4, 10, 61, 62]). It can be noted that, as regards the values of H_V and E, most HEA-based nitride and carbide films are not even inferior to usual nanocoatings with a few nanometers grains, let alone the multilayer (see Fig. 1) or multicomposite nc-(Al,Ti)N/a-Si_3N_4 coatings. In terms of a thermal stability comparison, reference can be made to the data of Ref. [62] suggesting that the (Ti – Al – Si)(C,N) coating maintains its initial hardness of about 42 GPa up to a temperature of 1200 °C. Thus, the films prepared on the base of refractory compounds can be made hard and thermally stable without necessarily resorting to the high entropy factor but rather employing traditional nanostructuring and doping techniques.

The exploitation of HEAs as metallic cermet microcomposite bindings is discussed in a number of publications (see, for example, Refs [63–66]). The properties of the composites Ti(C,N) – (Al,Co,Cr,Fe,Ni) and Ti(B,C) – (Co,Cr,Cu,Fe,Ni) are presented in Table 7 [63, 64].

References [63, 64] note that the mechanical properties shown in Table 7 are superior to those of usual cermets, for example, of fast-cutting-steel-reinforced ones, and highlight the high air oxidation resistence [65] and good tribological characteristics of HEA-containing composites. Finer grain ($L \sim 0.43$ μm) compositions were obtained for the composites TiC – 20 %$Co_{1.5}CrFeNi_{1.5}Ti_{0.5}$ prepared by liquid phase sintering at 1380 °C and exhibiting an ~ 10% higher hardness than that of commercial composites (16TiC – 2WC – 2TaC) – 20 % (5Co – 3Ni – 2Mo) with a grain size of ~ 0.9 μm [66]. It seems obvious that, thus far, little or nothing has been achieved in reinforcing cermets with HEAs.

2.5 Twinned structures

The effect of twinned and gradient structures on the properties of nanomaterials is reviewed in Ref. [67] together with some aspects of their preparation. The first to draw attention to the role of twinned structures were to a large extent the authors of Refs [68–70], who showed the following using nanocrystalline copper as an example:

- nanostructures can possess simultaneously high strength and high electric conductivity [68];
- the grain size and lamellate thickness are equivalent in terms of their effect on the strength; decreasing either of them increases both the strength and plasticity, consistent with the well-known Hall–Patch relation [69];
- films with a nanotwined structure have a far higher thermal stability than usual nanomaterials [70].

These characteristics of nanotwinned structures are due to features of the coherent lamellate interfaces that form from small-angle grain boundaries and which are characterized by a low boundary energy and a weak scattering of conduction electrons. It is also hypothesized in Refs [68, 71]

Table 7. Grain size and mechanical properties of HEA-bound cermet composites (σ_b is the flexural strength).

Cermet	L, μm	σ_b, GPa	E, GPa	H_V, GPa	K_{IC}, MPa m$^{1/2}$
Ti(C,N) – (Al,Co,Cr,Fe,Ni)	5 – 7	1.733	no data	1.787	11.4
Ti(B,C)$_{0.1-0.5}$ – (Co,Cr,Cu,Fe,Ni)	6 – 40	no data	234 – 261	4.19 – 9.14	no data

Table 8. Microhardness (H_V), crack resistance (K_{IC}), and oxidation onset temperature (T_{ox}) of nanocrystalline and nanotwinned BN and diamond samples.

Object	Structure		H_V, GPa	K_{IC}, MPa m$^{1/2}$	T_{ox}, °C
	Grain size L, nm	Lamella width λ, nm			
Nanocrystalline BN	~ 14	—	85	6.8	~ 1100
Nanotwinned BN	—	3.8	~ 110	12.7	~ 1300
Nanocrystalline diamond	10 – 30	—	110 – 140	5 – 15	~ 800
Nanotwinned diamond	—	~ 5	175 – 204	9.7 – 14.8	~ 1000

that the interaction of complete dislocations with small-angle boundaries causes a splitting according to the reaction $1/2\,[101] \rightarrow 1/6\,[1-21]+1/3\,[111]$, which produces slipping Shockley partial dislocations with a Burgers vector of 1/6 [1–21] that cross Frank dislocations with a Burgers vector of 1/3 [111]. The dislocations slipping along the lamellate boundaries ensure plasticity, whereas the crossing dislocations are responsible for the material strength. HRTEM studies [67] have confirmed the presence of Shockley and Frank dislocations on the interlamella boundaries and within lamellas, respectively.

Information on the role of twinned structures in high-melting-point compounds is as yet limited and mostly recent. The most significant results were reported for typical superhard materials: cubic boron nitride [72] and diamond [73], whose samples with a nanotwinned structure were prepared using onion-structured original nanoparticles consolidated at high pressures and high temperatures (P up to 25 GPa, and $T = 1800 - 2000\,°\mathrm{C}$) (Table 8).

Table 8 clearly demonstrates the advantage of nanotwinned structures with the lamella width λ by far less than the grain size L. Shown in Fig. 13 are the structure of twinned nanograins in BN, lamella width distribution by size, and the size dependence of the microhardness (note that in the last case the values of L and λ fit the curve equivalently, as also noted for metals [69]).

Data on nanotwinned structures in refractory carbides (see, for example, Refs [74–77]) are mostly still being collected. Thus, HRTEM data reveal the presence of two types of twinned (111) nanointerfaces for carbon and metallic sublattices (of a coherent and noncoherent nature, respectively) in the nonstoichiometric zirconium carbide $ZrC_{0.6}$ [74]. First principles calculations also showed that the ordering of carbon vacancies in this phase reduces the defect packing energy considerably compared to that for stoichiometric carbide.

The carbide solution (Ti, Zr)C exhibits, when annealed ($T \sim 1300\,°\mathrm{C}$), the formation of lamellar nanostructures in spinoidal decay products, which is accompanied by a 10% increase in hardness, an effect which can be used in the development of new types of solid alloys [75, 76].

A nanolaminated structure was also found in the *MAX* phase of Ti_3SiC_2 (layer thickness of 20–30 nm) obtained by self-propagating high-temperature synthesis [77]. Characteristically, fractography studies revealed the presence of bent laminated plasticity-revealing layers similar to those shown in Fig. 4.

3. Theoretical approaches

3.1 Electronic state and structure

Review [79] provides a comprehensive analysis of *ab initio* quantum chemistry simulations of the electronic structure, chemical bonding, and some properties of carbide silicide Ti_3SiC_2. There is a large amount of literature (see, for example, Refs [2, 7, 78, 79]) in which quantum-chemical approaches are applied in a variety of approximate forms to the description of the electronic state and structure of high-melting-point compounds. By now, theoretical approaches have been expanded and enhanced, considerably widening the range of potential objects for study. Molecular dynamics (MD) methods, the density functional theory (DFT), and similar approaches are widely used for predicting electronic spectra, structure, phase transitions, physicochemical and

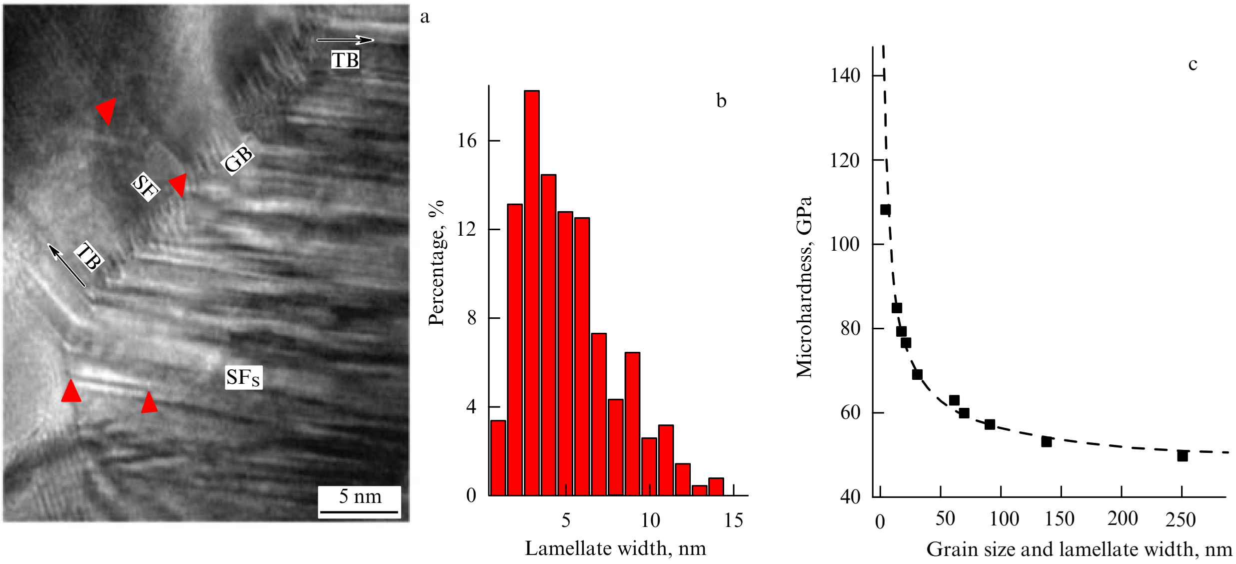

Figure 13. HRTEM images of nanotwins in boron nitride (a), distribution of widths of twinned lamellates by size (b), and microhardness as a function of grain size and lamellate width (c) [72].

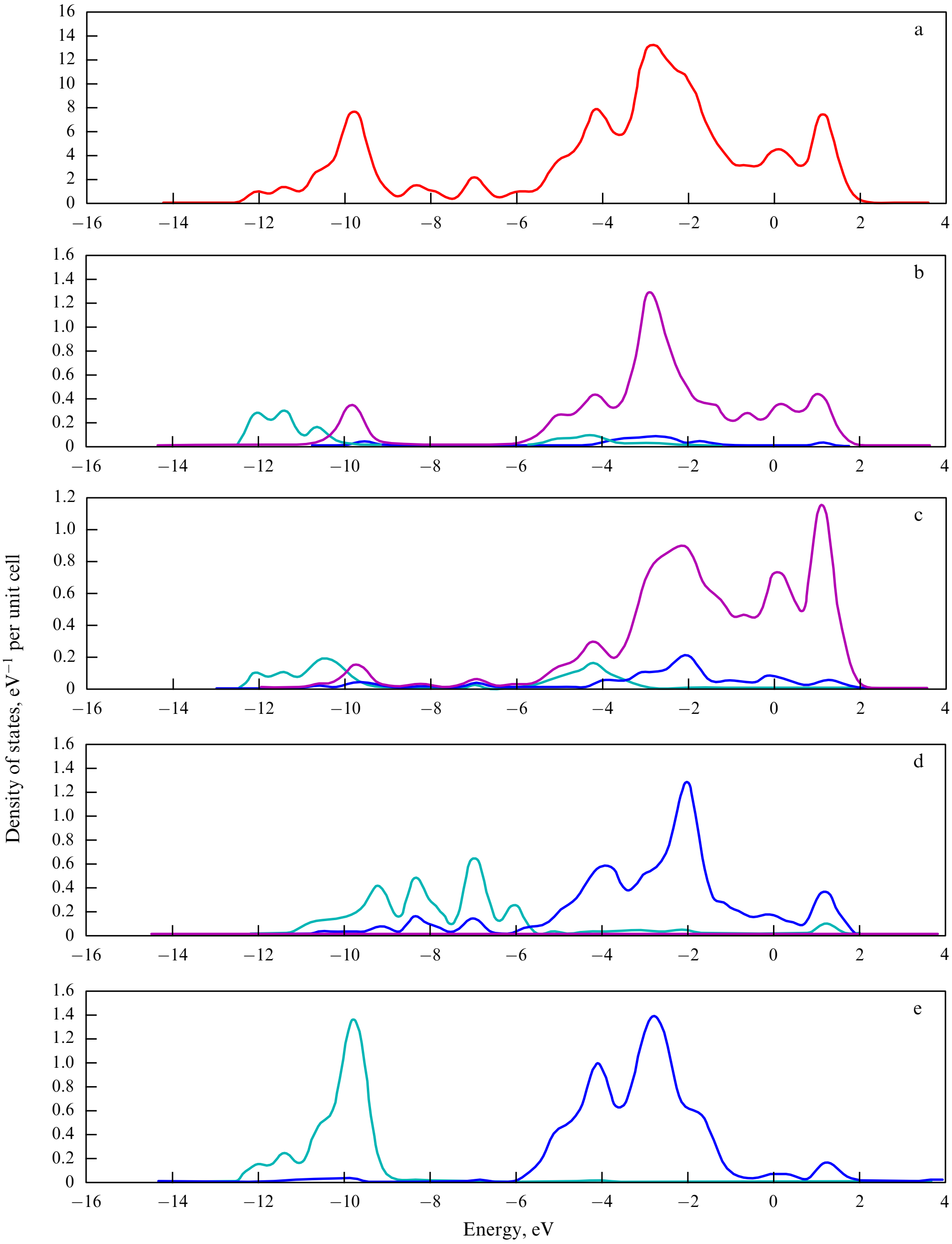

Figure 14. Total (a) and partial (b–e) densities of electronic states in Ti_3SiC_2; (b, c) two positions of atoms Ti (see Fig. 2b), (d) Si, and (e) C.

physicomechanical properties, and stability under extreme conditions (including thermal, radiation, stress–strain, and corrosion effects). While referring the reader to earlier work [9, 10] for the general issue of the behavior of nanomaterials under extreme conditions, here we will confine ourselves to the most typical examples involving some of the novel objects described in Section 2.

Figure 14 presents the total and partial densities of states for titanium carbide-silicide Ti_3SiC_2 [80]. The DFT data in Fig. 14 suggest the absence of a band gap in and the metallic nature of this compound, in good correlation with the electron heat capacity and resistivity values (see Table 1). The hybridization of the valence band states of $Ti_2 3d - Si 3p$ and $Ti_{1,2} 3d - C 2p$ (in the −6 to −1 eV energy range) is evidence of the covalent $Ti_{1,2} - C$ and $Ti_2 - Si$ bonds, correlating with a high Young's modulus.

Reference [81] combined a first principles DFT method with empirical MD to examine the 1D-BN–1D–Si nanoheterostructures for their electronic structure and thermal conductivity features. It was found that, due to noncovalent interlayer couplings, a weak interaction occurs between layers with a weak interlayer electron transport, with the Si and BN layers dominating the electron transport and the phonon transport, respectively (the heat flux for these layers being six times larger). The results obtained on the asymmetric transport of electrons and phonons in the nanocomposite 1D-BN–1D-Si suggest a high potential for application of such heterostructures in thermoelectric devices.

The prediction of stable structures for the systems $Hf-C$, $Ti-N_2$, $B-C-O_2$, and $C-N_2$ was obtained with USPEX (Universal Structure Prediction Evolutionary Xtallography) [82–85], a method which traces the evolution of the energetic

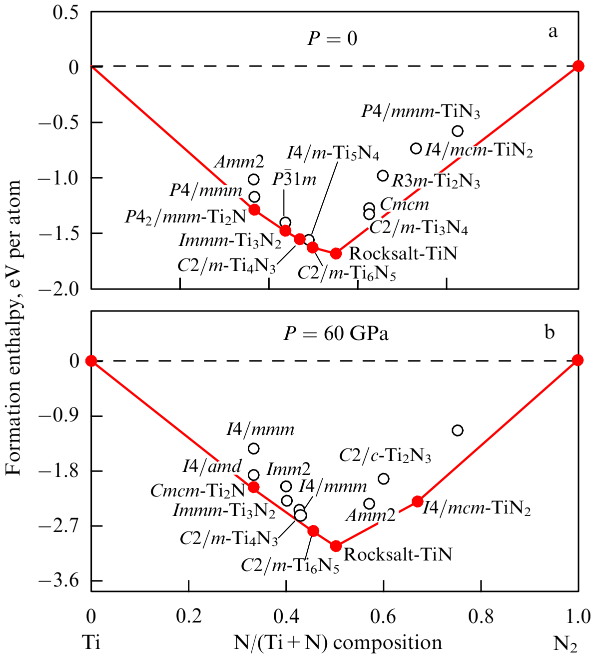

Figure 15. Change in the phase formation enthalpy (space group shown) as a function of composition for the titanium–nitrogen system at 0 GPa (a) and 60 GPa (b). Stable phases are marked by solid dots.

characteristics as functions of composition, pressure, and some other parameters. Figure 15 depicts as an example the change in the formation entropy for various compositions of titanium nitride [83].

From the data in Fig. 15, the phases that can be considered stable are NaCl-structured TiN and tetragonal ε-Ti_2N, as indeed observed in many experiments, and also some other new phases, such as orthorhombic Ti_3N_2, cubic TiN_2, and monoclinic Ti_4N_3 and Ti_6N_5, which were not reported in earlier X-ray phase analyses. Using *ab initio* DFT (including both the local density and generalized gradient approximations), data on the electronic states (similar to those shown in Fig. 14) were calculated and mechanical properties evaluated for all the nitride phases mentioned (TiN, Ti_2N, Ti_3N_2, Ti_4N_3, Ti_6N_5, and TiN_2).

A similar amount of research has been done on the predicted stable phases in the form of well-known hafnium monocarbide HfC and predicted new carbides Hf_3C_2 and Hf_6C_5 [82], as well as a new phase B_4CO_4 [84] and many superhard carbon–nitrogen compounds [85]. The application of DFT to calculating two-dimensional *MX* phases is described in Ref. [86], which studied the stability of carbide phases $M_2^{\mathrm{I}}M^{\mathrm{II}}C_2$ and $M_2^{\mathrm{I}}M_2^{\mathrm{II}}C_2$, where M^{I} and M^{II} are group IV–VI transition metals of the Periodic Table.

3.2 State diagrams

References [87–89] used the simplest possible regular solution approximation including the nanosize effect to estimate the eutectic temperature decrease in carbide (nitride)–boride type pseudobinary systems using the TiC(TiN) − TiB_2 and B_4C − TiB_2 composites as the examples. A reduction in the eutectic temperature of the system B_4C − TiB_2 (which is 2310°C in coarse grain samples) is shown in Table 9 as a function of the grain size for various assumed grain boundary energies [88]. While the data of Table 9 cannot claim to be anything more than estimates, they seem to be useful for determining the working temperature ceilings of carbide–boride nanocomposites.

Table 9. Estimates of the reduction in the eutectic temperature in nanostructured TiB_2 − B_4C films.

Surface energy on grain boundaries, J m^{-2}	Approximate reduction in eutectic temperature (K) for various grain sizes *L*	
	L = 5 nm	*L* = 10 nm
3	1000	500
2	670	340
1	140	170

The high-temperature decomposition of cubic titanium–aluminum nitride $Ti_{1-x}Al_xN$ was considered in Ref. [90] in terms of spinoidal and bimodal decays. Using *ab initio* DFT approach, the authors calculated the temperature dependence of the formation enthalpy and came to the conclusion that the high-temperature applicability conditions for these nitride coatings due to the high decay temperature can be calculated more accurately. A detailed study of the spinoidal and bimodal decays of the $(Zr_{1-x}Al_x)_2O_3$ phase for monoclinic and hexagonal modifications was carried out in Ref. [91] using DFT and thermodynamic simulation methods. The authors note the possible formation of nanocomposite oxides as a result of the decay and point to about a twofold increase in hardness, which is important for the design of new superhard tool materials with high oxidation resistance.

Reference [75] used DFT to estimate the excess heat of mixing and spinoidal decay conditions for the TiC–ZrC system.

DFT/MD calculations of the electronic structure of phases in Hf–C and Hf–Ta–C systems were aimed at estimating more accurately the formation of the compound $HfTa_4C_5$ (HfC − 4TaC) with the melting point of ~ 4215 K exceeding that for individual TaC and HfC carbides [92]. Historically, these studies find their origin in an old (1930) paper [93] in which the highest melting points were reported for the HfC–TaC and TaC–ZrC systems (Fig. 16).

With the search for supersonic aircraft materials for nose cones and sharp wing edges, there has been increasing interest recently in understanding the synthesis and properties of high-temperature phases (see, for example, Refs [95, 96]). The calculations done in Ref. [92], on the one hand, confirmed the experimental fact that the high melting point of the compound $HfTa_4C_5$ is due to the removal of carbon during melting and the formation of congruently high-melting-point nonstoichiometric $MeC_{\sim 0.82}$ carbide [94]. On the other hand, the same calculations predicted the existence in the Ta-Hf–C–N system of a new compound with a still higher (by about 200 K) melting point. According to Ref. [92], the following conditions are necessary for the formation of such phases in carbide systems: (1) a large number of strong chemical bonds among nearest- and next-to-nearest-neighbor atoms, ensuring significant covalent and ion bonding; (2) entropy contribution from carbon lattice vacancies, and (3) the possibility that the Fermi level between the bonding and antibonding states can be changed by doping.

References [97, 98] applied a thermodynamic approach to more accurately calculate the phase diagrams of B–C and CaO − ZrO_2 systems, taking into account in the latter case that nanocrystals are stable compared to their larger-size counterparts. Based on a comparison of various approaches to estimating the melting temperatures of graphene-like

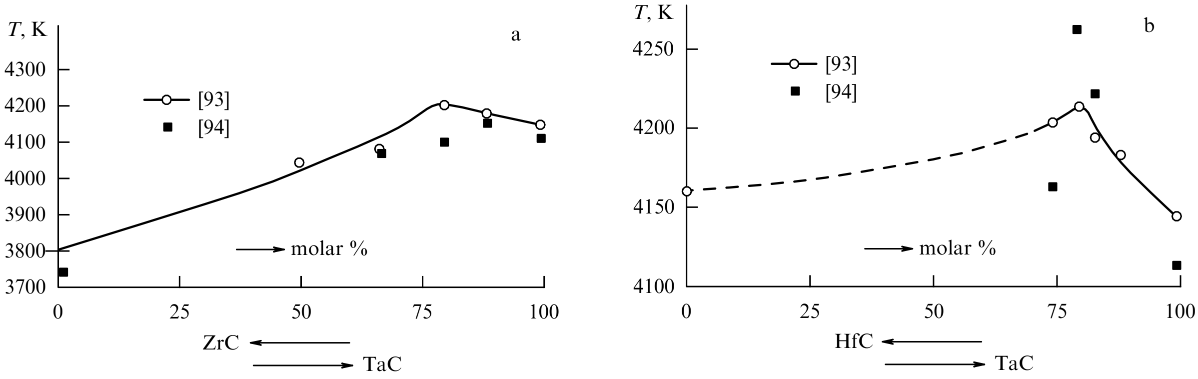

Figure 16. Melting points in systems TaC–ZrC (a) and HfC–TaC (b) [93, 94].

compounds BN, BP, AlN, SiC, etc., it was concluded that the thermal instability temperature of a two-dimensional hexagonal structure is given by the following expressions: $T_b \sim 10^4$ K$/a^2$ and $T_s \sim 2T_b/3$, where T_b and T_s are the melting point of the three-dimensional and two-dimensional objects, respectively, and a is the nearest neighbor distance in angströms [99]. Accordingly, two-dimensional high-melting point semiconductor type compounds should have the following T_s values: BN $\sim$ 2000 K; BP $\sim$ 2000 K; AlN $\sim$ 1600 K, and SiC $\sim$ 1900 K.

3.3 Deformation and radiation characteristics

As applied to the subjects reviewed, many of the theoretical MD and DFT estimates refer to stress–strain properties, for example, the elastic constants (C_{ij}), elastic (E) and shear (G) moduli, and volumetric strain (B), as well as the Poisson ratio (υ) and microhardness (H_V). As is known, these properties are important in a variety of strength calculations and, on the other hand, are closely related to the lattice energy and thermodynamic and thermal parameters. For some calculated results, a comparison with experimental data is evidenced in Table 10.

The microhardness estimates in Refs [82, 83] were based on the empirical relation $H_v = 2(k^2G)^{0.585} - 3$, where $k = G/B$. The two theoretical values shown for TiN [83] are due to using different versions of DFT (local density and generalized gradient approximations, the latter version yielding higher C_{ij}). From Table 10 it follows that the calculated and experimental data are, by and large, in satisfactory agreement for most of the characteristics considered. A similar agreement of theoretical results (obtained with different versions of DFT) with their experimental counterparts was observed by many researchers for hexagonal titanium diboride TiB_2 (see, for example, Refs [101, 102]).

Stress–strain property calculations for two-dimensional hexagonal structures using the features of the electronic energy spectra are discussed in detail in Refs [103, 104]. In particular, it is noted in Ref. [103] that a successive and consistent description of the elastic characteristics of covalent and ion-covalent crystals requires establishing more accurate interaction potentials and accumulating more experimental data. As applied to 2D structures and compared with the data of Refs [82, 83, 101, 102], the estimated characteristics, on the one hand, are narrower in range (often being limited to E alone) and, on the other hand, show a wide spread in values. Thus, for nanotube- or nanostrip-shaped hexagonal boron nitride, the following value ranges are provided for the Young's modulus: 693–1111 GPa (MD and DFT calculations) and 722–1220 GPa (experimental data) [104]. References [105–107] provide estimates for the elastic properties of two-dimensional MoS_2 type chalchogenides and BN–Mg and BN–C type nanocomposites. The maximum microhardness achievable for layered TiN/SiN_x nanoheterostructures was calculated with the aid of MD to have quite a large value of about 170 GPa [108]. The same study established that an extremely low impurity content is necessary.

DFT calculations of defect energies in nanolaminated Ti_3SiC_2 showed that the formation of vacancies and interstitial atoms in the silicon sublattice, and Ti $\rightarrow$ Si type substitutions are characterized by rather low energies, namely, 0.9 , 0.6, and 0.3 eV, respectively [109]. This suggests that the silicon planes (layers A in Fig. 2b) between the nanotwinned Ti_3C_2 structures are efficient sinks for radiation defects, ensuring the absence of amorphization during the irradiation by high-energy ions up to doses of $\sim$ 25 dpa [110] (see also Fig. 6).

Complex processes occurring during the irradiation of crystalline and nanocrystalline silicon carbide (SiC) are also being actively investigated by combining first principles

Table 10. Theoretical and experimental stress–strain characteristics of hafnium carbide and titanium nitride.

Object		Elastic constants, GPa			E, GPa	G, GPa	B, GPa	υ	H_V, GPa
		C_{11}	C_{12}	C_{44}					
HfC [82]	Calculations	589	98	192	no data	212	262	no data	33
	Experiment	500	no data	180	470	195	242	0.2 [1]	27 [1]
TiN [83]	Calculations	590; 704	145; 157	169; 183	466; 533	189; 215	294; 339	0.235; 0.238	22.6; 24.2
	Experiment	625	165	163	435 [1]	180 [1]	320	0.21 [1]	23

methods with HRTEM (see, for example, Refs [111–113]). It is shown that the large number of packing defects and twins in SiC nanosamples increases their stability against irradiation-induced amorphization considerably compared to carbide–silicon single crystals.

With the important features we have discussed, SiC- and Ti_3SiC_2-based materials are greatly promising candidates for a variety of applications as coatings, shells, matrices, etc. in fast and gas-cooled atomic reactors, as well as in ITER (International Thermonuclear Experimental Reactor) type fusion facilities. Clearly, more research is needed to make these innovations a reality, and in this context multiscale simulation, which has not yet been applied to refractory materials, also holds great promise.

4. Conclusions

The discussed examples of new experimental and theoretical approaches to the study of refractory compounds illustrate interesting results achieved in this area. Also discussed are the principles of the multilevel approach to the computer simulation of material stress–strain and failure processes [114]; data on the deformation of brittle materials (see, for example, Refs [115, 116]); the surge of interest in zirconium carbide as a basis for promising materials for new generation atomic space technology [117–119]; the discovery of the existence at room temperature of new active slipping systems in the single crystals of ZrC and TaC ($\{1\text{-}10\}\langle 110\rangle$ and $\{001\}\langle 110\rangle$) [120, 121]. In particular, the discovery of new slip systems in normally brittle ZrC and TaC carbides offers the potential for using them as the basis for developing plastic nanolaminated materials, a possibility previously found for the *MAX* phases (see Fig. 4).

At this point, it is also worthwhile to note that the high electrical conductivity and wear resistance of these compounds [12] (see Table 1), the attractive electrochemical properties of *MX* phases [25], and the good biocompatibility of 2D-BN [31] make them promising candidates for use in such diverse areas as electrical engineering, present-day energy conservation systems, nanomedicine, etc. In principle, research into new refractory compounds has not only greatly improved our understanding of materials science fundamentals but also significantly expanded the application range of both traditional carbides, nitrides and borides, and their new associated phases.

By and large, refractory compounds remain a topic of current interest (ein Spitze topic, using the German expression) in the fields of materials physics and materials science.

Acknowledgments

The author is grateful for the financial support provided by the RAS Presidium Program No. 1. The assistance of V V Klyucharev and S V Klyucharev in arranging the review is appreciated.

References

1. Andrievski R A, Spivak I I *Prochnost' Tugoplavkikh Soedinenii i Materialov na Ikh Osnove* (Strength of Refractory Compounds and Their Related Materials) (Chelyabinsk: Metallurgiya, 1989)
2. Andrievski R A, Umanskii Ya S *Fazy Vnedreniya* (Interstitial Phases) (Moscow: Nauka, 1977)
3. Gusev A I, Rempel A A, Magerl A J *Disorder and Order in Strongly Nonstoichiometric Compounds: Transition Metal Carbides, Nitrides, and Oxides* (Berlin: Springer, 2001)
4. Andrievski R A *Russ. Chem. Rev.* **74** 1061 (2005); *Usp. Khim.* **74** 1163 (2005)
5. Mayrhofer P H, Mitterer C, Clemens H *Adv. Eng. Mater.* **7** 1071 (2005)
6. Pogrebnjak A D et al. *Phys. Usp.* **52** 29 (2009); *Usp. Fiz. Nauk* **179** 35 (2009)
7. Ivanovskii A L *Prog. Mater. Sci.* **57** 184 (2012)
8. Gusev A I *Phys. Usp.* **57** 839 (2014); *Usp. Fiz. Nauk* **184** 905 (2014)
9. Andrievski R A *Phys. Usp.* **57** 945 (2014); *Usp. Fiz. Nauk* **184** 1017 (2014)
10. Andrievski R A, Khatchoyan A V *Nanomaterials in Extreme Environments: Fundamentals and Applications* (Springer Series in Materials Science, Vol. 230) (Cham: Springer, 2016)
11. Barsoum M W, El-Raghy T *J. Am. Ceram. Soc.* **79** 1953 (1996)
12. Barsoum M W *MAX Phases: Properties of Machinable Ternary Carbides and Nitrides* (Weinheim: Wiley-VCH, 2013)
13. Radovic M, Barsoum M W *Am. Ceram. Soc. Bull.* **92** (3) 20 (2013)
14. Barsoum M W, Radovic M *Annu. Rev. Mater. Res.* **41** 195 (2011)
15. Tallman D J et al. *Acta Mater.* **85** 132 (2015)
16. Du Y et al. *J. Am. Ceram. Soc.* **83** 197 (2000)
17. Samsonov G V, Vinitskii I M *Handbook of Refractory Compounds* (New York: IFI. Plenum, 1980); Translated from Russian: *Tugoplavkie Soedineniya* (Moscow: Metallurgiya, 1976)
18. Andrievski R A *Russ. Chem. Rev.* **78** 821 (2009); *Usp. Khim.* **78** 889 (2009)
19. El Saeed M A, Deorsola F A, Rashad R M *Int. J. Refract. Met. Hard Mater.* **41** 48 (2013)
20. Prikhna T A et al. *J. Superhard Mater.* **34** 102 (2012); *Sverkhtverd. Mater.* (2) 38 (2012)
21. Prikhna T A et al. *Adv. Sci. Technol.* **89** 123 (2014)
22. Prikhna T A et al. *Solid State Phenomena* **230** 140 (2015)
23. Tallman D J et al. *J. Nucl. Mater.* **468** 194 (2016)
24. Andrievski R A et al. *Neorgan. Mater.* **14** 675 (1978)
25. Naguib M et al. *Adv. Mater.* **26** 992 (2014)
26. Halim J et al. *Chem. Mater.* **26** 2374 (2014)
27. Ghidiu M et al. *Chem. Commun.* **50** 9517 (2014)
28. Come J et al. *Adv. Energy Mater.* **6** 1502290 (2016)
29. Novoselov K S *Rev. Mod. Phys.* **83** 837 (2011); *Usp. Fiz. Nauk* **181** 1299 (2011)
30. Rao C N R, Ramakrishna Matte H S S, Maitra U *Angew. Chem. Int. Ed.* **52** 13162 (2013)
31. Pakdel A, Bando Y, Goldberg D *Chem. Soc. Rev.* **43** 934 (2014)
32. Lin Y, Connell J W *Nanoscale* **4** 6908 (2012)
33. Meziani M J et al. *ChemPhysChem* **16** 1339 (2015)
34. Chen Y (Ed.) *Nanotubes and Nanosheets: Functionalization and Applications of Boron Nitride and Other Nanomaterials* (Boca Raton, FL: CRC Press. Taylor and Francis Group, 2015)
35. Li L H, Chen Y *Adv. Funct. Mater.* **26** 2594 (2016)
36. Li C et al. *Nanotechnology* **20** 385707 (2009)
37. Green J F, Bolland T K, Bolland J W *J. Chem. Phys.* **64** 656 (1976)
38. Wei X et al. *Adv. Mater.* **22** 4895 (2010)
39. Yu Y et al., in *Nanotubes and Nanosheets: Functionalization and Applications of Boron Nitride and Other Nanomaterials* (Ed. Y Chen) (Boca Raton, FL: CRC Press. Taylor and Francis Group, 2015) p. 525
40. Eliseeva N S et al. *JETP Lett.* **95** 555 (2012); *Pis'ma Zh. Eksp. Teor. Fiz.* **95** 633 (2012)
41. Wu R et al. *Prog. Mater. Sci.* **72** 1 (2015)
42. Yeh J W et al. *Adv. Eng. Mater.* **6** 299 (2004)
43. Yeh J-W *Ann. Chim. Sci. Mater.* **31** 633 (2006)
44. Yeh J W et al. *Mater. Sci. Forum* **560** 1 (2007)
45. Murty B S, Yeh J-W, Ranganathan S *High-Entropy Alloys* (Amsterdam: Elsevier, 2014)
46. Pogrebnjak A D et al. *Russ. Chem. Rev.* **83** 1027 (2014); *Usp. Khim.* **83** 1027 (2014)
47. Zhang Y et al. *Prog. Mater. Sci.* **61** 1 (2014)
48. Yeh Y-W *JOM* **67** 2254 (2015)
49. Lai C-H et al. *Surf. Coat. Technol.* **201** 3275 (2006)
50. Chang H-W et al. *Thin Solid Films* **516** 6402 (2008)
51. Lin C H, Duh J G, Yeh J W *Surf. Coat. Technol.* **201** 6304 (2007)
52. Tsai C-W et al. *Thin Solid Films* **520** 2613 (2012)
53. Huang P-K, Yeh J-W *J. Phys. D* **42** 115401 (2009)
54. Tsai M-H et al. *J. Phys. D* **41** 235402 (2008)

55. Firstov S A et al. *Powder Metallurg. Met. Ceram.* **52** 560 (2014); *Poroshk. Metallurg.* (9–10) 93 (2013)
56. Pogrebnjak A D et al. *Tech. Phys.* **60** 1176 (2015); *Zh. Tekh. Fiz.* **85** (8) 72 (2015)
57. Pogrebnjak A D et al. *Phys. Solid State* **57** 1559 (2015); *Fiz. Tverd. Tela* **57** 1529 (2015)
58. Shen W J et al. *J. Electrochem. Soc.* **160** C531 (2013)
59. Shen W-J, Tsai M-H, Yeh J-W *Coatings* **5** 312 (2015)
60. Braic V et al. *Surf. Coat. Technol.* **211** 117 (2012)
61. Cavaleiro A, de Hosson J T M (Eds) *Nanostructured Coatings* (Heidelberg: Springer, 2006); Translated into Russian: *Nanostrukturnye Pokrytiya* (Moscow: Tekhnosfera, 2011)
62. Shtansky D V et al. *Surf. Coat. Technol.* **206** 4840 (2012)
63. Zhu G, Liu Y, Ye J *Mater. Lett.* **113** 80 (2013)
64. Cheng J et al. *Surf. Coat. Technol.* **281** 109 (2015)
65. Zhu G, Liu Y, Ye J *Int. J. Refract. Met. Hard Mater.* **44** 35 (2014)
66. Lin C M et al. *JOM* **66** 2050 (2014)
67. Andrievski R A *Rev. Adv. Mater. Sci.* **45** 335 (2016)
68. Lu L et al. *Science* **304** 422 (2004)
69. Shen Y F et al. *Scripta Mater.* **52** 989 (2005)
70. Anderoglu O et al. *J. Appl. Phys.* **103** 094322 (2008)
71. Lu K, Lu L, Suresh S *Science* **324** 349 (2009)
72. Tian Y J et al. *Nature* **493** 385 (2013)
73. Huang Q et al. *Nature* **510** 250 (2014)
74. Hu W et al. *J. Appl. Cryst.* **46** 43 (2013)
75. Borgh I et al. *Acta Mater.* **66** 209 (2014)
76. Ma T et al. *Int. J. Refract. Met. Hard Mater.* **51** 25 (2015)
77. Vadchenko S G et al. *Nanotechnol. Russ.* **10** 67 (2015); *Ross. Nanotekhnol.* **10** (1–2) 57 (2015)
78. Toth L E *Transition Metal Carbides and Nitrides* (New York: Academic Press, 1971); Translated into Russian: *Karbidy i Nitridy Perekhodnykh Metallov* (Moscow: Mir, 1974)
79. Medvedeva R I, Enyashin A N, Ivanovskii A L *Zh. Strukt. Khim.* **52** 795 (2011)
80. Zhang H B, Bao Y W, Zhou Y C *J. Mater. Sci. Technol.* **25** 1 (2009)
81. Cai Y Q et al. *J. Appl. Phys.* **119** 065102 (2016)
82. Zeng Q et al. *Phys. Rev. B* **88** 214107 (2013)
83. Yu S Y et al. *Phys. Chem. Chem. Phys.* **17** 11763 (2015)
84. Wang S N et al. *Phys. Chem. Chem. Phys.* **18** 1859 (2016)
85. Dong H F et al. *Sci. Rep.* **5** 9870 (2015)
86. Anasori B et al. *ACS Nano* **9** 9507 (2015)
87. Andrievski R A *Zh. Vsesoyuz. Khim. Obshch. im. D I Mendeleeva* **36** 137 (1991)
88. Kalinnikov G V et al. *Phys. Solid State* **50** 374 (2008); *Fiz. Tverd. Tela* **50** 359 (2008)
89. Andrievskii R A, Kalinnikov G V *Russ. Chem. Bull.* **60** 1025 (2011); *Izv. Ross. Akad. Nauk. Ser. Khim.* (6) 1001 (2011)
90. Mayrhofer P H, Music D, Schneider J M *Appl. Phys. Lett.* **88** 071922 (2006)
91. Sheng S H, Zhang R F, Veprek S *Acta Mater.* **59** 3498 (2011)
92. Hong Q-J, van de Walle A *Phys. Rev. B* **92** 020104(R) (2015)
93. Agte C, Alterthum H *Z. Tech. Phys.* (6) 182 (1930)
94. Andrievski R A et al. *Sov. Powder Metallurg. Met. Ceram.* **6** (1) 65 (1967); *Poroshk. Metallurg.* **1** 85 (1967)
95. Simonenko E P et al. *Rus. J. Inorg. Chem.* **56** 679 (2011); *Zh. Neorg. Khim.* **56** 1763 (2011)
96. Patsera E I et al. *Ceram. Int.* **41** 8885 (2015)
97. Rogl P F et al. *Calphad* **44** 3 (2014)
98. Drazin J W, Castro R H R *J. Am. Ceram. Soc.* **99** 1778 (2016)
99. Davydov S Yu *Semicond.* **49** 1634 (2015); *Fiz. Tekh. Poluprovodn.* **49** 1683 (2015)
100. Chen X-Q et al. *Intermetallics* **19** 1275 (2011)
101. Kumar R et al. *Comput. Mater. Sci.* **61** 150 (2012)
102. Sun L et al. *J. Alloys Comp.* **579** 457 (2013)
103. Davydov S Yu, Posrednik O V *Phys. Solid State* **57** 837 (2015); *Fiz. Tverd. Tela* **57** 819 (2015)
104. Kumar R, Parashar A *Nanoscale* **8** 22 (2016)
105. Liu K, Wu J *J. Mater. Res.* **31** 832 (2016)
106. Kvashnin D G et al. *Phys. Chem. Chem. Phys.* **18** 965 (2016)
107. Zhang J, Wang C *J. Phys. D* **49** 155305 (2016)
108. Ivashchenko V I et al. *Thin Solid Films* **578** 83 (2015)
109. Zhang H B et al. *J. Nanomater.* **2013** 831590 (2013)
110. Whittle K R et al. *Acta Mater.* **58** 4362 (2010)
111. Zhang Y W et al. *Phys. Chem. Chem. Phys.* **14** 13429 (2012)
112. Wang X et al. *Acta Mater.* **99** 7 (2015)
113. Imada K et al. *J. Nucl. Mater.* **465** 433 (2015)
114. Psakh'e S G *Herald Russ. Acad. Sci.* **83** 260 (2013); *Vestn. Ross. Akad. Nauk* **83** 398 (2013)
115. Ovid'ko I A, Skiba N V, Sheinerman A G *Phys. Solid State* **50** 1261 (2008); *Fiz. Tverd. Tela* **50** 1211 (2008)
116. Gutkin M Yu, Ovid'ko I A *Phys. Solid State* **52** 718 (2010); *Fiz. Tverd. Tela* **52** 668 (2010)
117. Lanin A *Nuclear Rocket Engine Reactor* (Springer Series in Materials Science, Vol. 170) (Heidelberg: Springer, 2013)
118. Katoh Y et al. *J. Nucl. Mater.* **441** 718 (2013)
119. Zheng M-J, Szlufarska I, Morgan D *J. Nucl. Mater.* **471** 214 (2016)
120. Kiani S et al. *Phil. Mag.* **95** 985 (2015)
121. Kiani S et al. *Scripta Mater.* **100** 13 (2015)